Available online at www.sciencedirect.com

jmr&t Journal of Materials Research and Technology

journal homepage: www.elsevier.com/locate/jmrt

Original Article

Characteristics of dynamic softening during high temperature deformation of CoCrFeMnNi high-entropy alloy and its correlation with the evolving microstructure and micro-texture

Sumit Ghosh [a], *Madan Patnamsetty* [b,*], *Mahesh C. Somani* [a], *Pasi Peura* [b]

[a] *Materials and Mechanical Engineering, Centre for Advanced Steels Research, University of Oulu, 90014, Finland*
[b] *Materials Science and Environmental Engineering, Tampere University, 33720, Tampere, Finland*

ARTICLE INFO

Article history:
Received 23 September 2021
Accepted 18 November 2021
Available online 25 November 2021

Keywords:
High entropy alloys
Plastic flow
Dynamic recrystallization
Critical stress/strain
Kinetic model
Micro–texture

ABSTRACT

The characteristics of dynamic recrystallization (DRX) of a CoCrFeMnNi high–entropy alloy (HEA) was investigated via hot compression testing in the temperature range 950–1100 °C and at true strain rates of 10^{-2} and 10^{-1} s^{-1}. The discontinuous DRX was found to be the dominant mechanism corroborating the microstructural evolution. The progress of the initiation of DRX was investigated in terms of critical strain/stress required using the Poliak–Jonas analytical criterion. Consequently, a new kinetic model based on Avrami–type function was established for the HEA to predict the DRX fractional recrystallization. It was revealed that the volume fraction of DRX grains increased with increasing strain. In the case of 10^{-2} s^{-1}, steady–state flow was achieved after the completion of one DRX process cycle resulting in further straining, leading to the occurrence of dynamic restoration processes involving formation of substructures and generation and annihilation of dislocations inside the DRX grains which effectively increased the fraction of partially deformed DRX (substructured) grains. A good agreement between the proposed DRX kinetics model and microstructure observation results validated the accuracy of DRX kinetics model for CoCrFeMnNi HEA. The preferred orientation of the non–recrystallized grains was towards the formation of <101> fiber texture, whereas a random micro–texture is revealed in the recrystallized grains.

1. Introduction

High entropy alloys (HEAs) as hypothesized by Yeh et al. [1], are complex multi–principal elemental alloys, containing four or more principal alloying elements that form simple solid solutions. Murthy et al. [2] contemplates the novel concept of HEA design as the renaissance in metallurgy that created a worldwide drive for alloy design in a path–breaking manner in the history of metallurgical research. The initial design

* Corresponding author.
E-mail address: madan.patnamsetty@tuni.fi (M. Patnamsetty).
https://doi.org/10.1016/j.jmrt.2021.11.089

approach of HEAs was to attain a single–phase alloy through high configuration mixing entropy [1]. However, a review report by Miracle and Senkov [3] explains the emergence of new design concepts enabled facilitation of multicomponent alloy systems that have shown new paths of research to explore a wide range of astonishing properties achievable through proper alloy design. In addition, George et al. [4] reviewed a significant number of HEAs, and explained the enormous possibilities of compositional spaces to develop a combination of novel or advanced properties like high strength, improved fatigue resistance, high corrosion resistance, good damage tolerance etc. It is worth noting that these properties can change rapidly even with a small variation in the composition. The equiatomic, face centered cubic (FCC), single–phase solid solution, CoCrFeMnNi HEA was the first such example reported in 2004 and is termed as 'Cantor alloy' after its discoverer Prof. Brian Cantor [5]. Additionally, the Cantor alloy happens to be the most researched HEA, as the single–phase FCC based alloy is stable over a wide range of temperatures (~800–1200 °C) [4]. Thus, it has attracted enormous attention as a model HEA in order to gain a better understanding of the properties realizable on FCC based HEAs. In addition, a study by Li et al. [6] on the irradiation properties of Cantor alloy has also shown excellent irradiation resistance, suitable for nuclear industry.

Deformation processing of high entropy alloys (HEAs) can be challenging at elevated temperatures. Hence, a comprehensive understanding of the effects of processing parameters on deformation mechanisms is, vital since these in turn may significantly influence the microstructural evolution as well as resultant mechanical properties. Accordingly, optimized processing can facilitate the occurrence of safe microstructural mechanisms such as dynamic recovery (DRV) and DRX enabling microstructural reconstitution. The degree of occurrence of DRX process depends on the flow stress during deformation, for which the accuracy depends on the hot deformation parameters, i.e., strain, strain rate, and temperature. In a previous study on the evaluation of hot deformation characteristics of Cantor alloy at different strain rates and temperatures by Patnamsetty et al. [7] has shown to experience various deformation mechanisms including the safe processing phenomena of DRX and DRV and also, the manifestation of adiabatic and/or localized shear bands depending on the processing parameters. In addition, a processing map of Cantor alloy was recently constructed at authors' laboratory [7] using the principles of dynamic materials modelling (DMM) in order to map and identify different deterministic domains in temperature–strain rate space characterizing various microstructural mechanisms operating in these domains as well as the regime marking the manifestation of instabilities that must be avoided for defect–free processing. Considering all the operating hot deformation mechanisms [7], it was clearly established that DRX was the dominant mechanism for a defect–free processing of the alloy. Accordingly, a DRX domain extending over the strain rate and temperature ranges of 10^{-2} –5 x 10^{-1} s^{-1} and 950–1100 °C, respectively, was considered 'safe' for hot working of the alloy. In addition, DRX expectedly played a vital role in reducing the deformation resistance and promoted grain refinement in the material through microstructural reconstitution. It is noteworthy that processing parameters, i.e., temperature, strain, and strain rate, significantly affect the DRX grain size and its volume fraction. Therefore, models describing the kinetics of DRX and evolution of dynamically recrystallized grain structures and corresponding sizes should be developed in order to characterize the DRX behavior during the hot deformation process. Additionally, the DRX process normally occurs in low stacking fault energy (SFE) materials [8]. In this context, the Cantor alloy was reported to be a low SFE material at room temperature [9]. However, based on *ab initio* calculations, Huang et al. [10] showed that the SFE increased with the increase in temperature of the alloy.

To achieve the desired mechanical behavior and to control the microstructural homogeneity, the understanding of the microstructural evolution is very essential. On the other hand, the mechanical properties are also influenced by the micro–texture evolution, which in turn is associated with the microstructural evolution. Both the texture as well as microstructural reconstitution is governed by DRX, which in turn determines the final properties of metals and alloys. There are only few studies that have reported the crystallographic texture evolution during the mechanical processing of Cantor alloy. For instance, studies on cold rolling [11], severe plastic deformation [12] as well as rotary swaging [13] of Cantor alloy have all shown the evolution of brass type texture, which is common in low SFE alloys and this behavior is related to the evolution of deformation twins. The annealing treatments of cold rolled Cantor alloy [11] has resulted in static recrystallization with the microstructure changes occurring in the form of grain boundary (GB) nucleation and annealing twinning. Additionally, the nuclei formed along these GBs has retained the rolling textures, whereas the formation of annealing twins was associated with a randomized texture. Eleti et al. [14] stated the formation of weak textures during the hot deformation of Cantor alloy at 800, 900 and 1000 °C and strain rates 10^{-3}, 10^{-2} and $1s^{-1}$ in both DRX and deformed (un–recrystallized) grains. Formation of weaker texture in the DRX grains is attributed to a subsequent increase in the fraction of annealing twins during hot deformation that randomizes the orientation of the DRX grains. However, no clear explanation was mentioned about the formation of weak texture in the un–recrystallized grains. Further statistical experiments were suggested in the same study by Eleti et al. [14] to confirm the texture evolution of the un–recrystallized grains. On the other hand, Soares et al. [15] reported the evolution of <101> fiber texture along the compression axis (in the deformed grains) during compression testing conducted at a very high strain rate (2800 s^{-1} at room temperature). There are not many studies on kinetic modelling of DRX behavior of FCC based HEAs. Therefore, the current investigation has addressed the following objectives.

The objectives of the current investigations are as follows:

(i) To determine the critical conditions for the commencement of DRX within the safe workability domain (deformed at 950–1100 °C and 10^{-2} – 10^{-1} s^{-1} strain rates) using the criteria proposed by Poliak and Jonas [16], where critical stress and strain necessitated for the initiation of DRX process are established from

the inflection point on the strain hardening rate (θ) *vs.* flow stress (σ) curve;

(ii) Establishing a model to elucidate the kinetics of DRX using an Avrami–type function encompassing different deformation conditions;

(iii) Characterization of associated microstructural changes as a result of DRX accompanied by changes in the flow stress that requires careful analysis both before and after the compression testing, particularly in respect of grain structure evolution and corresponding size, volume fraction of DRX grains, occurrence of twinning, and misorientation distribution of the substructure along different deformation conditions; and

(iv) Determination of the characteristics of micro–texture formation following the DRX process as a function of the variation in processing conditions, viz., strain rate and temperature. In particular, the evolution of micro–texture components and substructures of the dominantly oriented grains, need to be characterized following the completion of DRX.

2. Experimental details

2.1. Materials and methods

A ~2 kg ingot (~140 × 40 × 40 mm^3) of CoCrFeMnNi HEA, comprising of 20 at. % of each alloying element was drop cast using high purity elemental powders via melting in a vacuum induction melting furnace at SWEREA AB, Sweden. The HEA was homogenized at 1150 °C for 12 h in argon atmosphere and cooled to room temperature inside the furnace. The homogenized HEA was hot rolled at 1000 °C in multiple passes with a reduction of ~10% per pass, to a final thickness of ~11 mm. During hot rolling, the HEA was reheated in the furnace after each pass to maintain the selected rolling temperature. Finally, cylindrical specimens of dimensions ~ φ8 × 10 mm were extracted from hot rolled plate in the traverse – normal direction via electric discharge machining (EDM), as shown in the flow chart (Fig. 1). These specimens were uniaxially hot compressed according to a test plan using a Gleeble® 3800 thermomechanical simulator. The schematic of the experiments conducted in the Gleeble is shown in Fig. 1. The data corresponding to the DRX domain, as delineated in the processing maps (i.e., strain rate of $10^{-2} - 10^{-1}$ s^{-1} and temperature ranges of 950–1100 °C respectively) developed by Patnamsetty et al. [7] were considered in the current article, to evaluate and model the DRX kinetics as a function of processing parameters.

2.2. Material characterization

For the EBSD studies, the hot compressed samples were sliced at center-plane towards the compression axis (CA) and the respective specimens were polished using standard metallographic technique. The final stage of polishing was carried out using a non-crystallizing amorphous 0.02 μm colloidal silica suspension (MasterMet-2) to enable EBSD analysis. The EBSD data acquisition was done using a field emission scanning electron microscope (FE-SEM, Zeiss ULTRA Plus) equipped with a Symmetry® EBSD detector (Oxford instruments). The EBSD data was acquired at an acceleration voltage of 20 kV, covering an area of 600 μm × 600 μm with a step size of 0.7 μm, and analyzed using the HKL Channel 5 software. As normally interpreted, the grain boundaries (GBs) were categorized as high angle (HAGBs) and low angle grain boundaries (LAGBs) corresponding to the misorientation angle (φ) ranges $\varphi \geq 15°$ and $2° < \varphi < 15°$, respectively, to determine their characteristics in respect of microstructural evolution. The grain size was calculated considering the grains with HAGBs. Additionally, the GBs regions including Σ3 twin (CSL) GBs regions were disregarded from the grain size evaluations. Furthermore, the grain average misorientation (GAM) map was constructed from the EBSD data to characterize fully recrystallized, partially-deformed and deformed grains as per HKL Channel 5

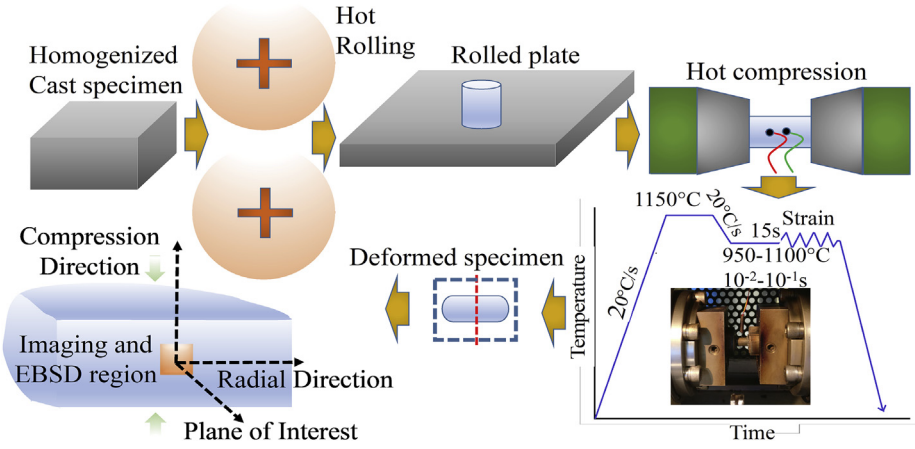

Fig. 1 – Flowchart showing the processing sequence of the experiments comprising hot rolling of as-cast Cantor alloy, sample extraction, hot compression testing in Gleeble simulator and finally, sectioning for microstructural analysis in the region of interest.

manual using Tango software [17]. The grains with the GAM value < 2° and almost no LAGBs or subgrains inside them are illustrated as complete recrystallized grains, while the grains with the GAM value > 2° and mostly filled with LAGBs/subgrains, are designated as deformed grains. If the grain comprises of sub-grains, i.e., the GAM value is < 2°, but the misorientation between sub-grains is > 2°, then the respective whole grain is defined as substructured or partially-deformed grains [18]. The kernel average misorientation (KAM) is constructed to indicate the localized strain in the microstructures.

For the texture analysis, the inverse pole figures (IPFs) were evaluated for both recrystallized (includes the 'recrystallized' grains) and un-recrystallized (includes the 'deformed' and 'substructured' grains) fractions as per recrystallization fraction map considering the overall microstructure. For the contouring of the IPFs the halfwidth and cluster size were considered as 10° and 11°, respectively. The halfwidth controls the spread of the plane normal aligned with the specimen axes in the inverse pole figure. The cluster size represents the clustering of the same orientations thus speeding up the calculations as the software considers all the orientations and recognizes the clusters of same orientation (e.g., from the same grain) and substitutes the clusters by a single orientation with an increased weight.

3. Results and discussion

3.1. Flow stress behavior

Typical true stress *vs.* true strain curves, plotted using the data from the hot compression tests of CoCrFeMnNi HEA in the strain rate and temperature ranges of 10^{-2} – 10^{-1} s^{-1} and 950–1100 °C, respectively, are shown in Fig. 2. At all the test conditions, the flow stress values increased with increase in strain rate and decrease with increase in temperature. It is clearly visible that for all test conditions, the flow stress rises to a maximum value typical of peak stress (σ_p) behavior, followed by flow softening on further straining. This is typically a behavior of low SFE alloy implying the possible occurrence of DRX mechanism [14]. Initially, at low strains, work hardening is the governing mechanism operating during the hot deformation, resulting in accumulation and multiplication of dislocations. During this time, the flow stress increases abruptly, as the cross slip of screw dislocations (mechanical recovery) is sluggish. This is due to the low SFE value of the current HEA. Eleti et al. [14] reported a similar flow behavior of Cantor alloy. Consequently, the DRX occurs in HEAs following continued straining, since it is difficult to recombine the Shockley partials into initial perfect dislocations. Accordingly, the extent of cross slip and dynamic recovery in FCC based HEAs is relatively low. Therefore, the density of dislocations keeps increasing during hot deformation thus generating a driving force to initiate the DRX process. As the density of dislocations reaches a critical value, the DRX process is commenced and the work hardening rate starts to decrease significantly reaching the σ_p, beyond which the flow stress drops leading to softening. According to study by Varela-Castro et al. [19] on the critical strain (ε_c) required for the commencement of DRX of different steels is slightly lower than the peak strain (ε_p) and is normally ~0.7–0.9 times the ε_p. The softening of flow curve is due to the large-scale annihilation of dislocations due to the microstructural reconstitution through the formation of DRX grains [20]. Finally, a steady-state condition of flow curve is achieved, whereby an equilibrium is reached between the concurrent work hardening and dynamic softening processes. Referring to Fig. 2b, the true stress–strain curves of the samples deformed at 10^{-2} s^{-1} strain rates and at 1100, 1050 and 1000 °C temperatures, show that the flow curves initially rise to the σ_p conditions corresponding to the peak strains of ~ 0.18, 0.20, 0.23 respectively (as shown in Table 1), beyond which the flow stress curves show flow softening and gradually reach steady-state behavior at the true strains of ~ 0.45, 0.5 and 0.6, respectively. On further straining, the flow stress curve largely tends to remain as steady-state, which is attributed to the competition of work hardening during hot deformation with the simultaneous softening via the occurrence of DRV and DRX leading to microstructural reconstitution, a similar behavior is observed by Ghosh et al. [21] during the hot deformation of Ti + Nb stabilized IF steel. In the current case of the test at 950 °C, the peak strain can be discerned from the curve, but the steady-state strain could not be reached at least up to the experimental strain of ~ 0.7.

On the other hand, at 10^{-1} s^{-1} (Fig. 2a), the steady–state behavior could not be reached for all the hot compression tests in the temperature range 950–1100 °C up to ε ~ 0.7,

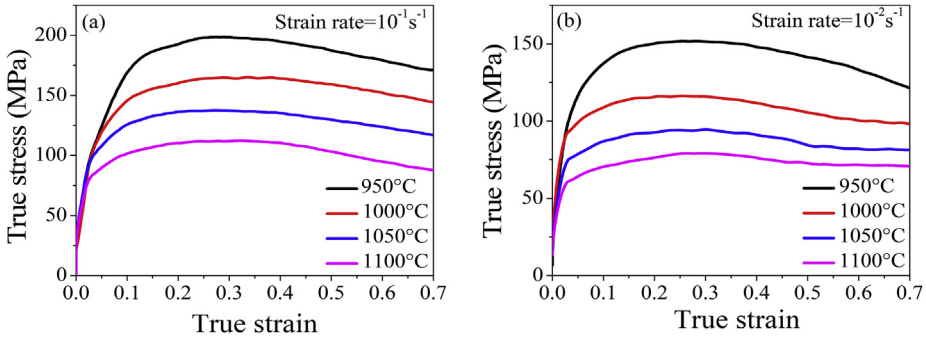

Fig. 2 – True stress *vs.* true strain curves of the HEA at various temperatures recorded at the strain rates (a) 10^{-1} and (b) 10^{-2} s^{-1}.

Table 1 – Experimental parameters corresponding to the occurrence of DRX in Cantor alloy and corresponding values of n_c and k estimated at different test conditions.

Strain rate (s^{-1})	Temperature (°C)	σ_c (MPa)	σ_p (MPa)	ε_c (MPa)	ε_p (MPa)	n_c	k
10^{-1}	950	183	199	0.24	0.27	2.6	0.36
	1000	160	165	0.20	0.25	4.3	0.13
	1050	130	137	0.13	0.22	3.3	0.18
	1100	99	112	0.09	0.20	4.7	0.16
10^{-2}	950	143	152	0.14	0.26	3.9	0.12
	1000	112	116	0.12	0.23	3.4	0.19
	1050	85	90	0.10	0.20	4.3	0.17
	1100	71	81	0.08	0.18	2.5	0.22

though the σ_p behavior is clearly evident, marking the peak strains of ~ 0.27, 0.25, 0.22 and 0.20 occurring at 950, 1000, 1050 and 1100 °C, respectively (Table 1). Referring to tests at 10^{-1} s^{-1}, it should be noted that the continuous decrease in flow stress up to ~0.7 strain at all temperatures without reaching the steady-state is an indication of incomplete DRX. A study by Quan et al. [22] on hot deformation of 3Cr20Ni10W2 alloy at 930 °C shows the similar result of incomplete DRX.

3.2. *Identification of critical strain/stress values for the onset DRX*

As explained above, the DRX process is initiated after exceeding the required critical strain/stress value in a flow curve. Before the σ_p value is reached, the work hardening occurs in respect of increase in dislocation density, i.e., the flow stress increases till reaching the peak strain. Thereafter, dynamic softening behavior dominates over work hardening rate, which eventually decreases the flow stress values. Therefore, it is obvious that the σ_p behavior during the isothermal compression is associated to the DRX process [23]. But it is generally difficult to recognize the flow stress corresponding to the initiation of DRX process from the true stress–strain curve. Therefore, a criterion proposed by Poliak and Jonas [16] can be used to determine the critical strain/stress required to initiate the DRX. This criterion is based on the change in strain hardening rate (θ) as a function of flow stress (σ). Accordingly, the σ_p value corresponds to the intersection of the plot of θ *vs.* σ, at $\theta = 0$, whereas the critical stress (σ_c) value for the commencement of DRX process is the inflection point as shown in Fig. 3b, d.

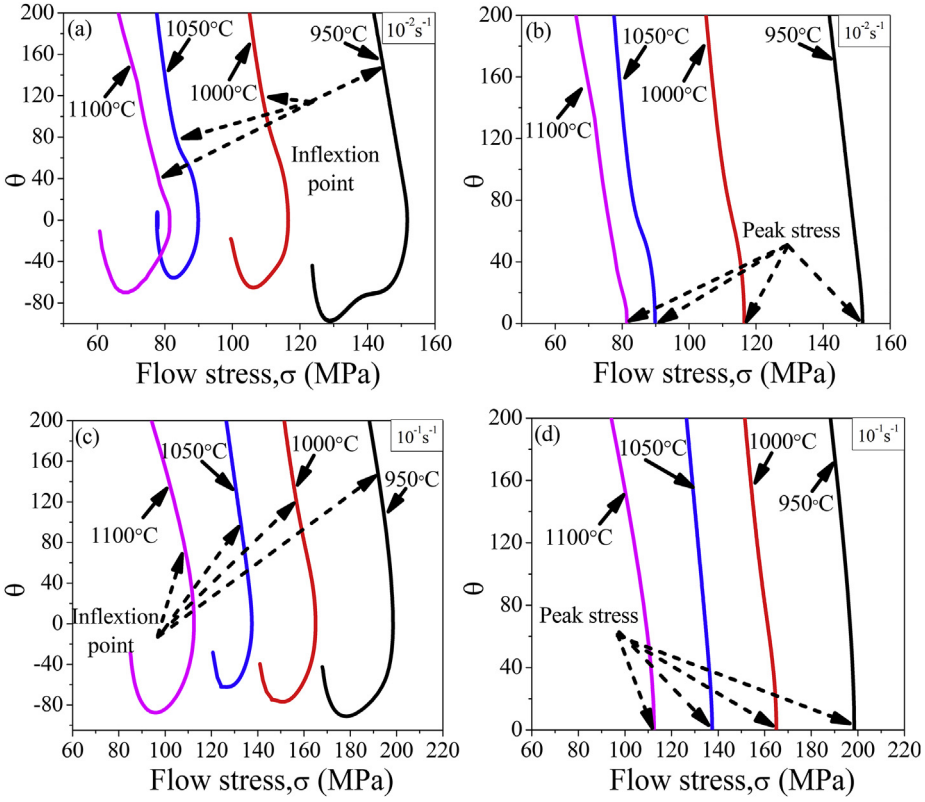

Fig. 3 – θ *vs.* σ curves of hot deformed HEA at different temperatures in the range 950–1100 °C and at strain rates (a & b) $10^{-2}s^{-1}$ and (c & d) $10^{-1}s^{-1}$.

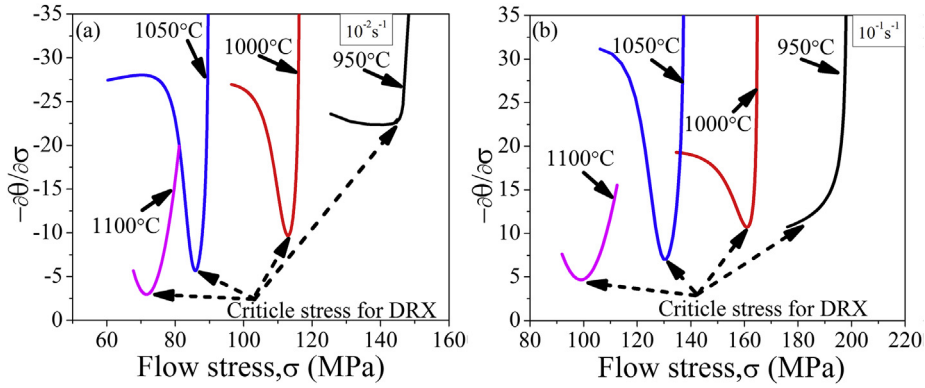

Fig. 4 – ∂θ/∂σ vs. σ curves steel at temperatures 950–1100 °C and strain rates (a) $10^{-2}s^{-1}$ and (b) $10^{-1}s^{-1}$.

In order to derive the strain hardening rate, $\theta = (\partial\sigma/\partial\varepsilon)_{\dot{\varepsilon}}$, the respective experimental flow curves were smoothened using a fast fourier transform (FFT) filter. Further, the variation of calculated strain hardening rate (θ) was plotted against flow stress (σ), as shown in Fig. 3a-d. Ryan and McQueen [24] explains that the work hardening curves (Fig. 3a, c) are comprised of two stages: firstly, the rate of work hardening dropped rapidly due to dynamic recovery and secondly, the slope of the curve changed sharply representing the DRX initiation. In addition, the extrapolation from the inflection point $\theta = 0$ during this second stage is the saturation stress (σ_{sat}) that relates to the softening due to DRV. The softening due to DRX is the difference between the σ_{sat} and σ from the flow curve.

It is hard to derive an exact inflection value, as shown in Fig. 3a and c. Therefore, an analytic approach proposed by Poliak and Jonas [16] to identify the inflection point is considered. In this approach, a second derivative of θ (generated from Fig. 3a-d) is plotted against the σ (i.e., $\partial\theta/\partial\sigma$ *vs.* σ). The generated data at all the test conditions (as shown in Fig. 4), provide the exact values of σ_c. The minima in these curves for the respective temperatures and strain rates represent the corresponding σ_c values. Therefore, the evaluated critical strain (ε_c) can be easily used to identify the σ_c values from the respective flow curves.

3.3. DRX kinetics

3.3.1. Strain analysis to identify the maximum dynamic softening

In order to identify the strains at which the dynamic softening rates are maximized, the work hardening rates were plotted against true strains, based on the flow stress curves recorded at 1100, 1050, 1000 and 950 °C for both strain rates (10^{-1} and 10^{-2} s^{-1}), as shown in Fig. 5a, c, e, and g, respectively. The minima (minimum point in the curve) in these individual plots correspond to the respective strains (ε^*) at which the dynamic softening rates are maximized. It can be seen that the ε^* expectedly rises with decreasing deformation temperature and increasing strain rate. In addition, the work hardening rate tends to increase back to $\theta = 0$ at the end of the DRX cycle, after reaching this minimum. Therefore, the θ *vs.* ε plots can be used to define the start of the steady-state strain.

From θ *vs.* ε plots (Fig. 5a), it is noticed that θ values became zero, implying that DRX was complete at both strain rates at 1100 °C. However, at 900 °C, strain hardening rate did not

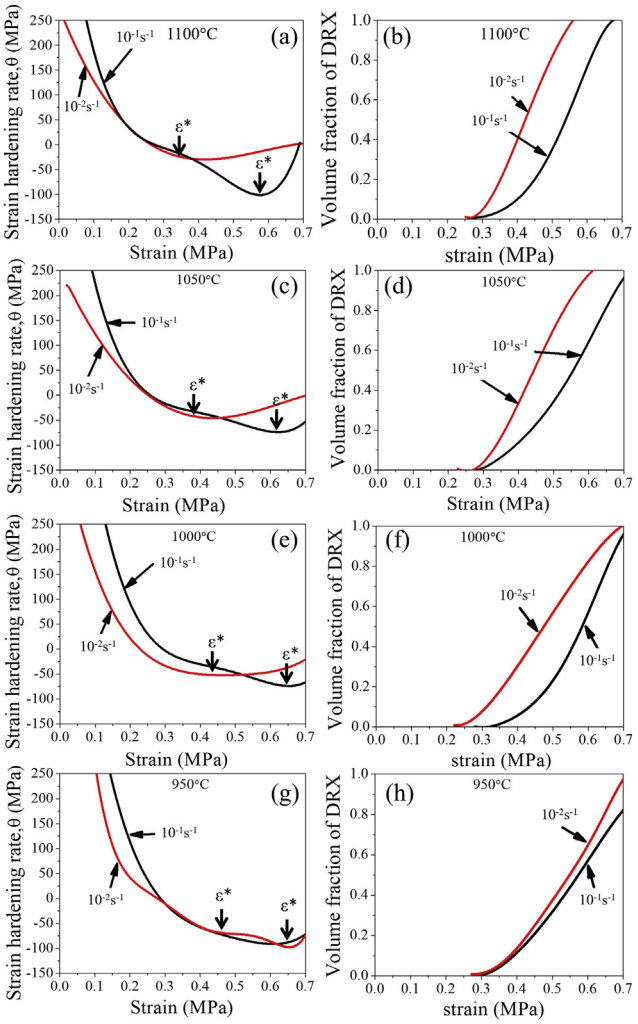

Fig. 5 – Strain hardening rate (θ) *vs.* true strain (σ) curves at two strain rates $10^{-2}s^{-1}$ and 10^{-1} $s^{-1}$for the HEA plotted at different temperatures i.e. (a) 1100 °C, (c) 1050 °C, (e) 1000 °C, (g) 950 °C and corresponding estimated X_{DRX} values (b, d, f, h), respectively.

reach the point at $\theta = 0$, therefore the dynamic recrystallization was partial at the maximum strain imposed, i.e., ~ 0.7 strain. The calculated DRX parameters are listed in Table 1, which clearly depicts that at a given deformation temperature, the respective critical strain/stress values increase with the increasing strain rate and decreases with increase in temperature.

3.3.2. *Analysis of kinetic model of DRX*

The flow curves (Fig. 2) at all the test conditions clearly exhibited either DRX or partial DRX behaviors. Initially, the flow curve increases with increasing strain due to the work hardening. However, the DRX initiates with the nucleation of new strain free grains during the hot deformation and the work hardening rate starts to decrease due to the evolution of these new strain free grains (DRX grains). Therefore, the evolution of new DRX grains results in a consequent softening of the flow stress curves. The σ_p appears in the flow curve due to the decrease in flow stress (strain softening) on further straining. Finally, a dynamic equilibrium is achieved due to the balance between strain hardening and strain softening behaviors, as stated above. The difference between the DRX and the DRV curves, as schematically shown in Fig. 6, can be used to estimate the net softening fraction attributed to DRX.

The equation used to estimate the volume fraction of DRX (X_{DRX}) [25] can be expressed as follows:

$$X_{DRX} = (\sigma_{sat} - \sigma_P)/(\sigma_{sat} - \sigma_{ss}) \text{ for } \varepsilon \geq \varepsilon_c \quad (1)$$

where, σ_P, σ_{ss} and σ_{sat} are the peak stress, steady state-stress, and saturated stress, respectively, as schematically shown in Fig. 6. In the equation, the numerator $\sigma_{sat} - \sigma_P$ is flow softening and denominator $\sigma_{sat} - \sigma_{ss}$ signifies the max attainable softening (Fig. 6). Therefore, flow softening is closely related with the X_{DRX} value. As previously explained, the initiation of DRX occurs at the critical strain. It can be seen from Fig. 5b, d, f, and h that as the strain increases for a given condition, the X_{DRX} value increases and reaches a maximum value of 1. It is apparent that the strain required to reach the same amount of X_{DRX} value, increases with the decrease in deformation temperature. A similar trend is seen in Fig. 5 b, d, f, h, i.e., at the deformation temperature of 950 °C, the DRX is delayed to higher strains in comparison with the flow behavior at other three temperatures (1000, 1050 and 1100 °C). In contrast the X_{DRX} value increases with the decrease in strain rate at a constant strain and temperature. Therefore, a decrease in strain rate enhances the degree of DRX mechanism, thus leading to the decrease in flow stress values, which is also consistent with the current results.

Furthermore, the expression of X_{DRX} can be illustrated by an exponent-type Avrami equation as shown in Eq. (2) [25]:

$$X_{DRX} = 1 - \exp\left[-k\{(\varepsilon - \varepsilon_c)/(\varepsilon_p)\}^{n_c}\right] \quad (2)$$

Where, n_c is the Avrami exponent, k is a constant. On applying natural logarithm to Eq. (2) gives:

$$\ln\{-\ln(1 - X_{DRX})\} = \ln K + n_c \ln\{(\varepsilon - \varepsilon_c)/(\varepsilon_p)\} \quad (3)$$

The term $\ln\{-\ln(1-X_{DRX})\}$ was plotted against $\ln\{(\varepsilon - \varepsilon_c)/(\varepsilon_p)\}$, to estimate the n_c and k. For example, at 1050 °C/10^{-1} s^{-1}, the values of n_c and k were calculated to be 3.4 and 0.18, respectively, as shown in Fig. 7.

The estimated values of k and n_c at different deformation conditions are shown in Table 1. In addition, the average values of k and n_c were estimated to be about 3.6 and 0.19, respectively. Therefore, by substituting the average values of k and n_c in Eq. (3), X_{DRX} can be expressed as:

$$X_{DRX} = 1 - \exp\left[-0.19\{(\varepsilon - \varepsilon_c)/(\varepsilon_p)\}^{3.6}\right] \quad (4)$$

In order to validate the model equation (Eq. (4)) describing the volume fraction of DRX on further straining, the predicted results (Fig. 5b, d, g, h) were plotted together with the experimentally obtained data (Eq. (2)), as shown in Fig. 8(a-d). The model data (plots with symbols) is correlated very well with the experimental data (plotted with solid lines).

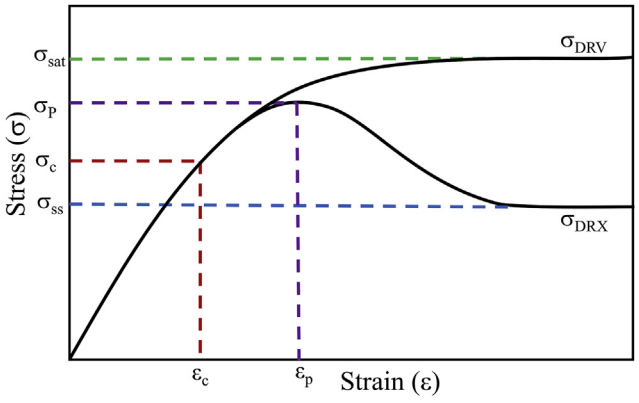

Fig. 6 – Schematic representation of DRX and DRV curves showing the strain/stress parameters used to determine the kinetics using Avrami–equations. σ_P, σ_{ss}, σ_c and σ_{sat} are the peak stress, steady-state stress, critical stress for the commencement of DRX and saturated stress respectively.

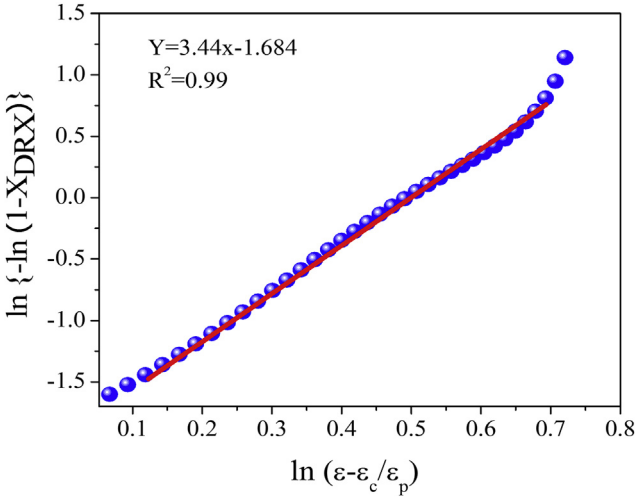

Fig. 7 – Linear fitting of data points from the $\ln\{-\ln(1-X_{DRX})\}$ vs. $\ln\{(\varepsilon-\varepsilon_c)/(\varepsilon_p)\}$ plot at $10^{-1}s^{-1}$/ 1050 °C to determine the n_c and k .

3.4. *Microstructural characterization and micro-texture analysis*

In this section, the characteristics of the microstructure and micro-texture evolutions, following the occurrence of DRX process in CoCrFeMnNi HEA at the stated test conditions are presented. The research investigations were conducted using the FESEM-EBSD. Both the evolution of micro-texture components as well as the characteristics of substructures examined in the grains of dominant orientation following the DRX process were determined. The microstructural evolution during hot deformation at various test conditions essentially mediated through the DRX mechanism, thus resulting in nucleation of fine, equiaxed grains along the pre-existing grain boundaries. The occurrence of DRX in low SFE materials is well-established and has been previously established for CoCrFeMnNi HEA [14].

3.4.1. *Initial material*

The as hot–rolled CoCrFeMnNi HEA prior to the isothermal compression experiments was examined for the starting microstructure using the EBSD; the data were acquisitioned in the plane normal to the rolling direction (i.e., parallel to the compression axis of the test samples). The microstructure as shown in Fig. 9a comprises equiaxed grains with an average grain size of ~ 18 μm (disregarding the Σ3 twin GBs). Figure 9 shows the inverse pole figure (IPF) map (Fig. 9a) with HAGBs (black color; $\varphi > 15°$) and image quality (IQ) map (Fig. 9b) with Σ3 twin boundaries (red color CSL boundaries) that are formed during hot rolling, making up a fraction of ~4%. Similarly, the green color boundaries are the LAGBs ($2 < \varphi < 15°$) make up for about ~52.5% of all boundaries. The inverse pole figure (Fig. 9c) shows that the <101> fiber was observed with an intensity around ~2.5 multiples of uniform density (MUD), which is a probability density defining the frequency of the occurrence of any given texture components.

3.4.2. *Effect of temperature and strain rate on the microstructure*

The microstructural evolution following the isothermal compression of the alloy to a true strain of ~0.7 has been further investigated using IPF color maps (as shown in Fig. 10). The average grain size (D) expectedly increased with an increase in deformation temperature and a decrease in strain rate (Table 2). In addition, it is known that the increase in deformation temperature enhances the degree of DRX because of enhanced GB mobility and this could accelerate the DRX process [26]. The formation of DRX nuclei which has been assumed to be dependent on the evolution of the substructure [27]. The dynamic balance between the DRX nucleation rate and grain boundary migration velocity could be achieved by two competing temperature activated processes, viz., bulk diffusion and grain boundary diffusion. According to Ravichandran and Prasad [28], DRX is consisting of two competing processes: interface formation (nucleus) and interface migration (growth). An interface can be expressed as a

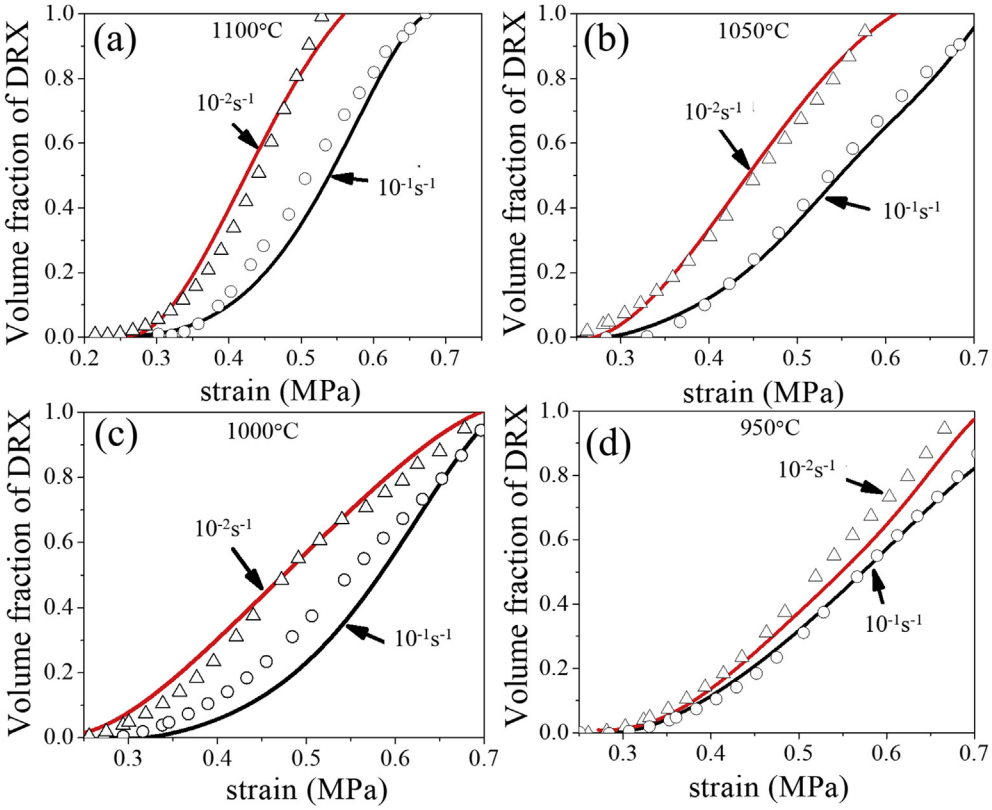

Fig. 8 – An assessment of the estimated X_{DRX} values (symbols) as a function of true strain (σ) in comparison with the experimentally obtained data (solid lines) at two different strain rates 10^{-2} and 10^{-1} s^{-1} and temperatures (a) 1100 °C, (b) 1050 °C, (c) 1000 °C and (d) 950 °C.

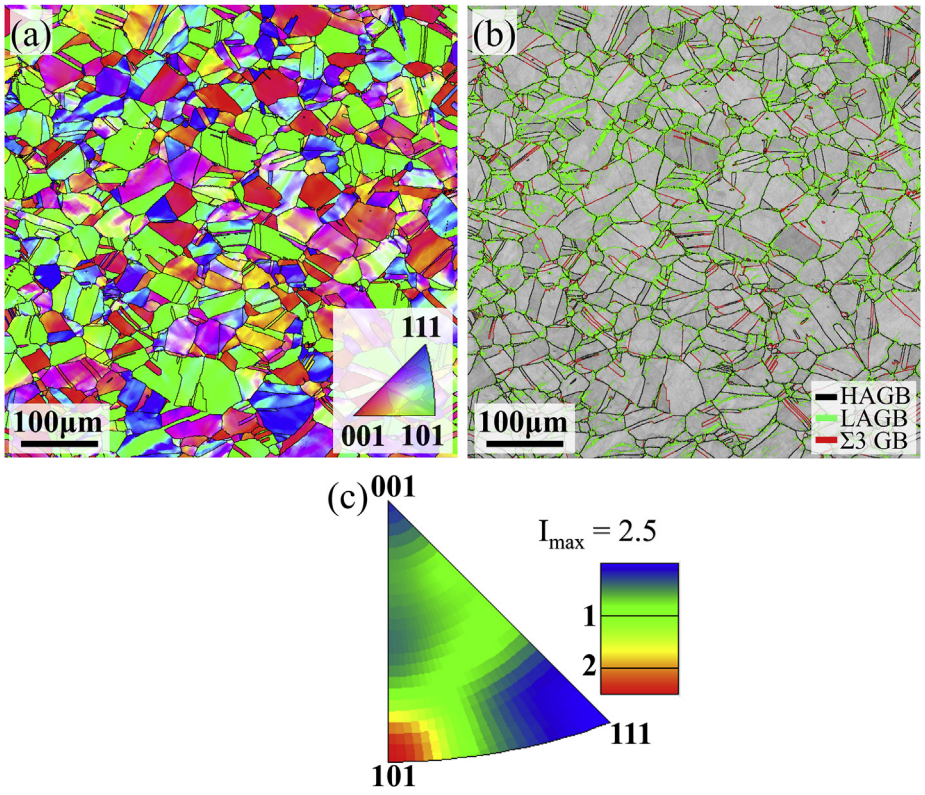

Fig. 9 – a) IPF map recorded on a plane parallel to the compression direction (CD); b) Band contrast image with HAGBs (φ >15°; black color), LAGBs (2 < φ < 15°; green color) and Σ3 twin GBs (red color); c) inverse pole figure parallel to compression axis.

boundary formed due to the generation of dislocation, recovery, and rearrangement, and further on attaining a certain configuration of large angle boundary (i.e., after the formation of nucleus) the respective interface will migrate. In DRX, the material acts as a power dissipator (no significant energy storage). When the interface formation and migration occur simultaneously, the DRX process is controlled by the slower one of these processes. If the interface formation rate is slower than migration rate, the material should experience certain strain before the critical configuration of the nucleus is achieved for migration, that leads to flow softening. A similar trend was observed in the X_{DRX} *vs.* ε plots, at two strain rates

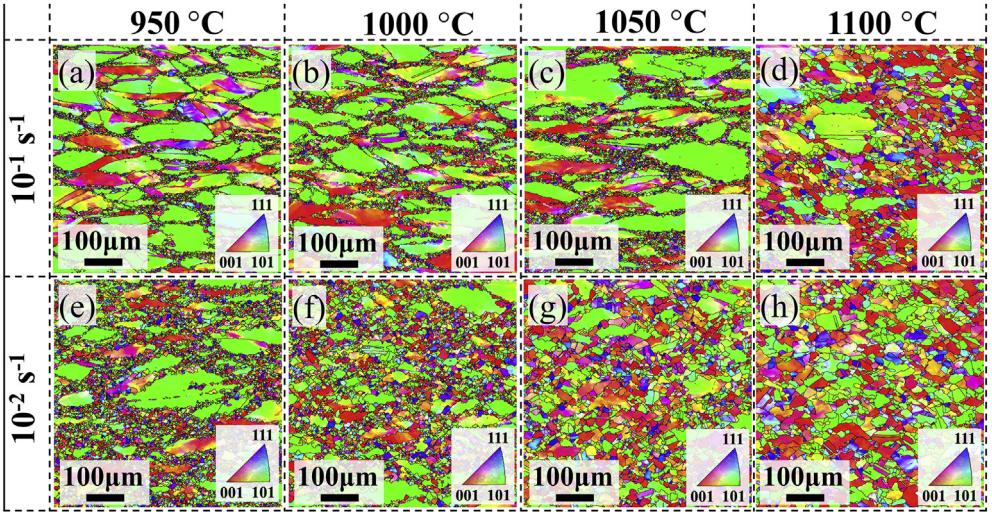

Fig. 10 – IPF color maps of the hot deformed CoCrFeMnNi HEA at different test conditions.

Table 2 – Grain size and grain boundaries evolution at different test conditions.

Strain rate (s^{-1})	Temperature (°C)	Average Grain Size (D μm)	D_{DRX} (μm)	$D_{unrecrystallized}$ (μm)	Recrystallization area fraction f_{DRX}	HAGBs	LAGBs	Σ3 Twin GBs
10^{-1}	950	5.58	4.21	6.82	11.10	46.83	53.17	2.96
	1000	6.20	5.35	7.93	22.10	57.57	42.43	5.33
	1050	5.70	5.18	6.79	25.50	43.66	56.34	6.39
	1100	13.78	10.79	18.72	39.20	70.67	29.33	10.60
10^{-2}	950	6.82	5.17	8.32	23.50	65.10	34.90	7.17
	1000	8.74	5.62	11.21	19.70	65.36	34.64	7.28
	1050	13.08	6.86	18.13	18.20	68.14	31.86	9.57
	1100	16.14	5.76	19.42	5.87	67.09	32.91	6.77

(Fig. 8). For instance, at 10^{-2} s^{-1}, the increase in temperature decreased the true strain value to complete the DRX, i.e., $X_{DRX} = 1$ signifying enhanced DRX kinetics. The sooner the DRX process is completed in respect of amount of strain, the faster the steady–state flow behavior is reached (as explained in section 3.1). However, at strain rate 10^{-1} s^{-1} and temperatures 950–1050 °C the X_{DRX} is < 1 which confirms the incomplete DRX process. In addition, the final X_{DRX} value at a true strain of ~0.7 (Fig. 8b – d) expectedly increases with the increase in temperatures, suggesting enhanced DRX process with increase in temperature.

In the current experiments at 10^{-1} s^{-1}, the LAGB fractions have evidently decreased with an increase in temperature. Figure 11a – d & 12a – d show the presence of LAGBs (as shown in Table 2) and local misorientation (KAM) along the boundaries of deformed grains. The respective LAGBs and local misorientations, typically account for the accumulation of dislocation density evolved during the hot deformation. The increase in temperature too increased the f_{DRX} value (The area fraction in the EBSD map comprising of defined DRX grains as shown in Fig. 13a - d) for reasons stated above, displaying large–scale elimination of dislocations into the formation of nuclei of DRX grains and accordingly, the fractions of LAGBs decreased with an increase in temperature. However, at 1050 °C/$10^{-1}$$s^{-1}$, there is a slight increase in LAGBs fraction, and their concentration is mostly along the GBs of the deformed grains (the local misorientation intensity as shown in Fig. 12c). This is tentatively due to the role of the GBs during the DRX process that may eventually lead to bulging of the GBs (nucleus) prior to the onset of DRX. However, the process needs to be confirmed, particularly in relation to the deformation conditions.

It is also known that Σ3 twin GBs are well associated with the DRX mechanism in low SFE materials. In addition, Kumar et al. [29] reported that the formation of Σ3 twin GBs reduces the boundary energy and facilitates enhanced GB mobility. In the current experiments, the increase in temperature (950–1100 °C) at 10^{-1} s^{-1} increased the fraction of Σ3 twin GBs (Table 2), which facilitated the occurrence of DRX mechanism and thereby increased the f_{DRX} values, too. Furthermore, the DRX grains at $10^{-1}$$s^{-1}$ (Table 2) showed a slight increment in average DRX grain size (D_{DRX}), varying marginally in the range from 4.2 to 10.8 μm with the increase in temperature from 950 to 1100 °C. At these temperatures, fine DRX grains were observed along the pre–existing GBs, as shown in Fig. 10a–d. Accordingly, a necklace type of microstructure is visible at these temperatures. Such a morphology of GBs confirms the primary nucleation mechanism (DRX) occurring during hot

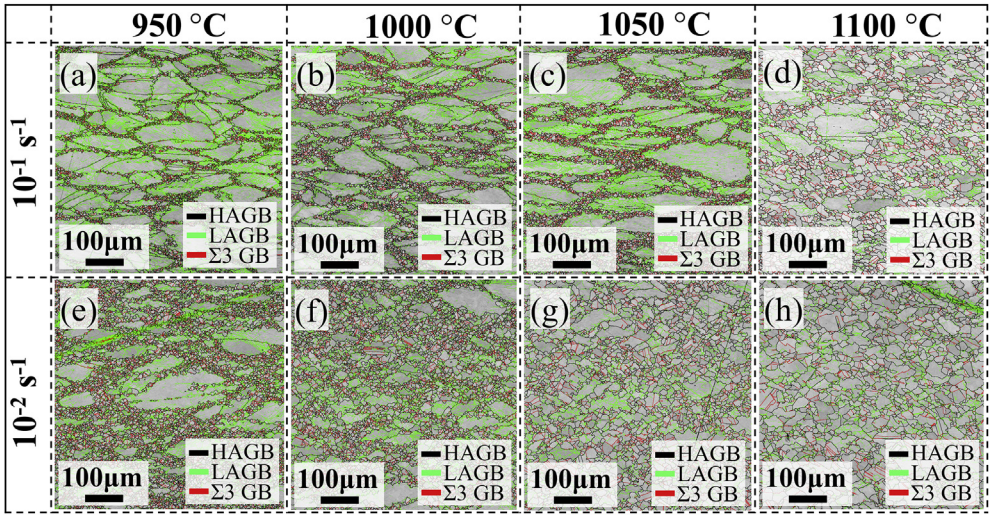

Fig. 11 – Image quality (IQ) maps highlighting HAGBs (solid black line), LAGBs (green lines) and Σ3 Twin GBs at different hot compression conditions.

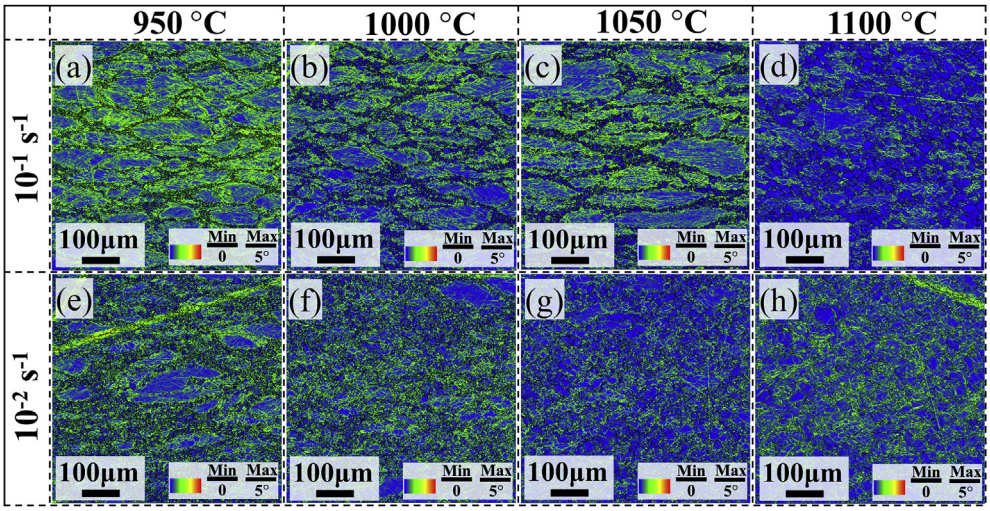

Fig. 12 – KAM profile of hot deformed CoCrFeNiMn HEA at different test conditions.

deformation is associated to discontinuous DRX (DDRX) [30]. Additionally, the progression of DDRX mostly occurs in the case of low SFE materials. The study by Huang and Logé [30] also suggests that when the stored energy in the low SFE materials exceeds the critical value, a new DRX grain is formed along the GBs through the conventional formation (nucleation) and migration (growth) of interfaces. At $10^{-1}s^{-1}$/1100 °C, the X_{DRX} value reached a maximum at ~0.7 strain, though the steady–state was apparently not yet reached at this strain. Hence, the DRX grains formed have not experienced any appreciable strain further. Therefore, there is no considerable number of dislocations generated in the DRX grains (as shown in Fig. 12d). Thus, we can see a sudden increment of f_{DRX} value and Σ3 twin GB fraction.

At $10^{-2}s^{-1}$, D_{DRX} varied in a narrow range (~5.2–6.9 μm) with the increase in deformation temperature (Table 2), and overall grain size slightly increased with increase in deformation temperature (~6.82–16.14 μm). At 950 °C/$10^{-2}s^{-1}$ the DRX nucleation is observed along the GBs of the initial grains, which resemble the necklace type microstructure that is associated with DDRX mechanism. In addition, the local misorientation profile (Fig. 12e) shows the accumulation of dislocations along the GBs of the deformed grains, which will eventually lead to the DDRX, though there is a competition between DRV and DRX. Additionally, the critical strain ε_c for the commencement of DRX at 950 °C/$10^{-2}s^{-1}$ is lower (0.14), as compared to 950 °C/$10^{-1}s^{-1}$ (0.24), and the f_{DRX} at 950 °C/$10^{-2}s^{-1}$ is greater (23.5%) as compared to 950 °C/$10^{-1}s^{-1}$ (11.1%), i.e., the DRX kinetics were enhanced at 950 °C/$10^{-2}s^{-1}$, due to the lower ε_c value and more time was required for straining due to lower strain rate. In addition, it is observed in Fig. 8d that at 950 °C for both the strain rates the DRX process is incomplete as the X_{DRX} value could not reach completion ($X_{DRX} < 1$). However, at ~0.7 ε the X_{DRX} of 950 °C/$10^{-2}s^{-1}$ is

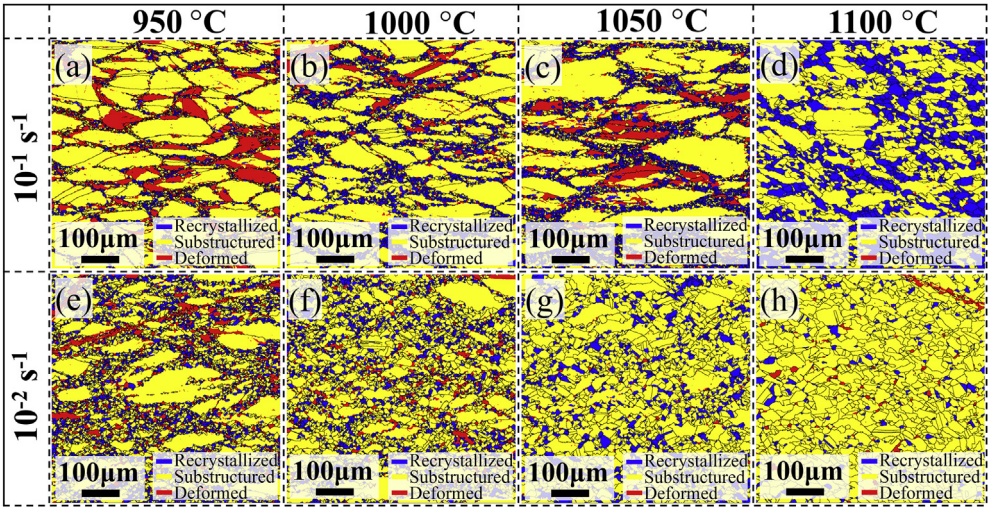

Fig. 13 – GAM maps highlighting recrystallized grains (blue color), sub–structured grains (yellow color) and deformed grains (red color) at different test conditions.

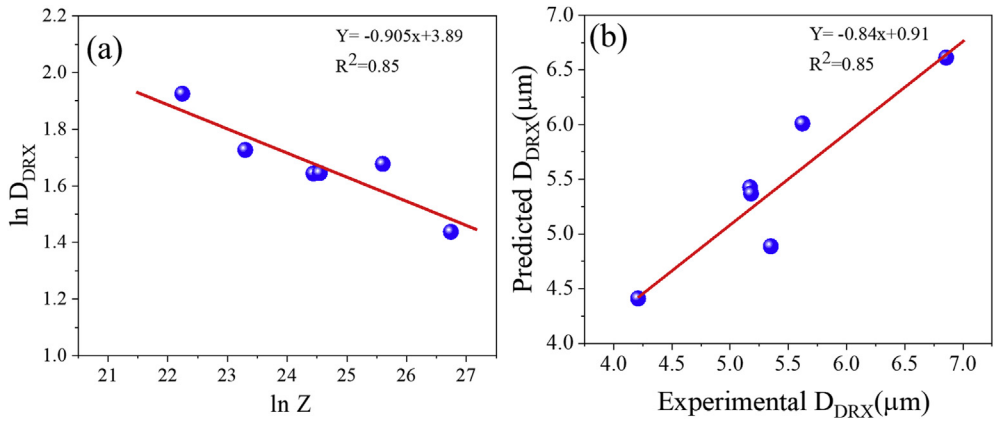

Fig. 14 – (a) Relationship between D_{DRX} and Z, (b) Experimental Vs. Predicted DRX grain sizes.

greater than the X_{DRX} corresponding to 950 °C/$10^{-1}s^{-1}$ displaying enhanced kinetics at lower strain rate.

Further, the true stress–strain curves for samples deformed at 1000, 1050 and 1100 °C temperatures and at a strain rate of 10^{-2} s^{-1} are flow softening type and tend to reach the steady-state after ~0.6, 0.5 and 0.45 strains respectively, which means that the first cycle of DRX process was completed, followed by continued nucleation and growth of new DRX grains during the steady-state regime on further straining. However, with further straining to experimental strain of about 0.7, the newly formed DRX grains also experienced intense dynamic recovery that involved in formation of substructures and generation and annihilation of dislocations causing dynamic equilibrium, which did change the misorientation profile of the newly formed grains. An interface forms because of dislocation generation, recovery and rearrangement and will migrate (nucleus) when it attains a configuration of large angle boundary. At lower strain rates, dynamic recovery significantly competes with DRX compared to that at high strain rates and hence, we can see the decrease in the number of grains with uniform orientation (blue colored) from the GAM/recrystallization fraction maps (Fig. 13 f-h). Therefore, at $10^{-2}s^{-1}$, regardless of the number of DRX cycles the specimen has gone through the given temperature the f_{DRX} values at the current final strain (~0.7 ε) decreased with increase in temperature. Similarly, the $\Sigma 3$ twin GBs, HAGBs and LAGBs showed varied narrow range values (as listed in Table 2) as the DRX grains experienced deformation on further straining.

From Fig. 13 it can be concluded that D_{DRX} values strongly depend on the strain rates as well as deformation temperatures, i.e., D_{DRX} should have a close relationship with Zener–Holloman (Z) parameter. The Z–parameter was evaluated at $\varepsilon = 0.7$, from the constitutive model of CoCrFeMnNi HEA [31]. The following equation [32] was used to build a mathematical model to be able to predict the DRX grain size:

$$D_{DRX} = A_{DRX}.Z^{n_{DRX}} \quad (5)$$

Where, D_{DRX} – average DRX grain size, A_{DRX}, n_{DRX} are material constants. In order to obtain the relationship between D_{DRX} and Z parameter, the D_{DRX} value from the specimens at temperature 950, 1000 and 1050 °C at both strain rates were selected. As shown in Fig. 14a the D_{DRX} can be presented as a power function of Z parameter as follows:

$$D_{DRX} = 49.15\ (Z^{-0.09}) \quad (5a)$$

The experimental and predicted DRX grain sizes are compared as shown in Fig. 14b. The established model well predicted the DRX grain size of the HEA. In addition, Table 3 shows the A_{DRX} and n_{DRX} of different steels and super alloys. A low value of n_{DRX} exponent suggests that the influence of Z parameter on D_{DRX} is very low. The Z parameter exponent (n_{DRX}) varies in a narrow range (−0.014 to −0.2956) regardless of the alloy type (Table 3) and all these values vary are in a narrow range suggesting low dependence of D_{DRX} on Z parameter.

3.4.3. *Microtextural evolution*

In the uniaxial compression tests, the preferred isothermal compression texture can be characterized by considering the compression axis as the reference direction. In this regard, the data from the EBSD measurements was used to construct the inverse pole figures (IPFs) and the respective IPFs are used to characterize the micro–textural evolution. The IPFs are evaluated separately for overall state (i.e., recry stallized + un–recrystallized grains), only the 'recrystallized' grains fraction (area of blue colored grains as shown in Fig. 13) as well as only the un–recrystallized grain fractions (i.e., including the area fraction of grains that are in red and yellow colors according to Fig. 13) at all deformation conditions, are shown in Fig. 15, Fig. 16, and Fig. 17, respectively.

Table 3 – Dependence of D_{DRX} on the Z parameter for different materials.

Alloy	A_{DRX}	n_{DRX}	References
CoCrFeMnNi	49.15	−0.09	Current work
UNS 6617 super alloys	9851.00	0.014	[32]
FGH96 superalloy	1730.00	−0.08	[33]
Medium carbon steel LZ50	98738.00	−0.2956	[34]
300 M steel	21000.00	−0.22	[35]
304 stainless steel	5200	−0.17	[36]
40Cr steel	6683.26	−0.0901	[37]

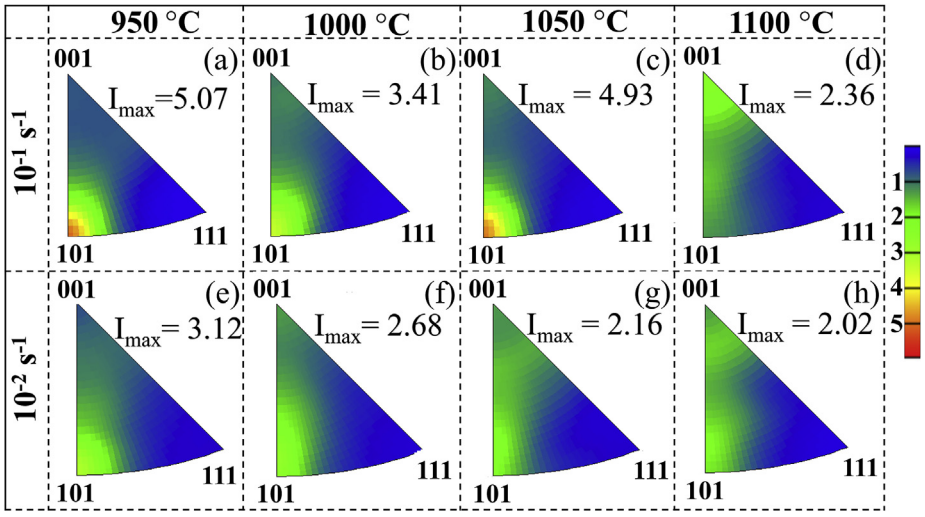

Fig. 15 – Over all IPFs obtained parallel to compression direction at different test conditions.

Additionally, the peak MUD values are shown for each IPF. The IPFs of recrystallized grains (Fig. 16) have shown weaker texture as expected, whereas the deformed texture is indicating <101> and <100> fiber textures. However, at 1100 °C/10^{-1} s^{-1}, the deformed texture is oriented mostly towards <100> fiber (though the MUD values point to a weak texture). It is presumed that an increase in the fraction of DRX grains (f_{DRX} = 39.2%) enabled a change in the crystal orientation. The IPFs of all the recrystallized grains are showing random texture due to the formation of Σ3 twin GBs, as large orientations change during the formation of Σ3 twins, a similar behavior of hot deformed Cantor alloy was explained by Eleti et al. [14]. Additionally, in the case of un–recrystallized grains (Fig. 17), a strong deformed texture is observed that is tending towards <101> fiber texture corresponding to all test conditions. The increase in temperature reduced the peak MUD values at both the strain rates. However, at test condition 1050 °C/$10^{-1}s^{-1}$, a higher MUD value is observed in comparison with the test condition 1000 °C/$10^{-1}s^{-1}$. The reason behind this is that in the case of un–recrystallized grains (Fig. 12c), the dislocation density was increased along the grain boundaries. This shows that an increase in concentration of dislocations will eventually lead to the formation of DRX grains on further straining. Additionally, in the orientation space, the texture components in the grains are formed in convergent regions of the velocity, i.e., even if the subgrain formation builds up the misorientations in the parent grain, the subgrains and the parent grains converge towards the same idea texture component (<101>component in the current case) [38].

The overall grain IPFs have shown similar texture when compared to recrystallized grains IPFs. This is due to the

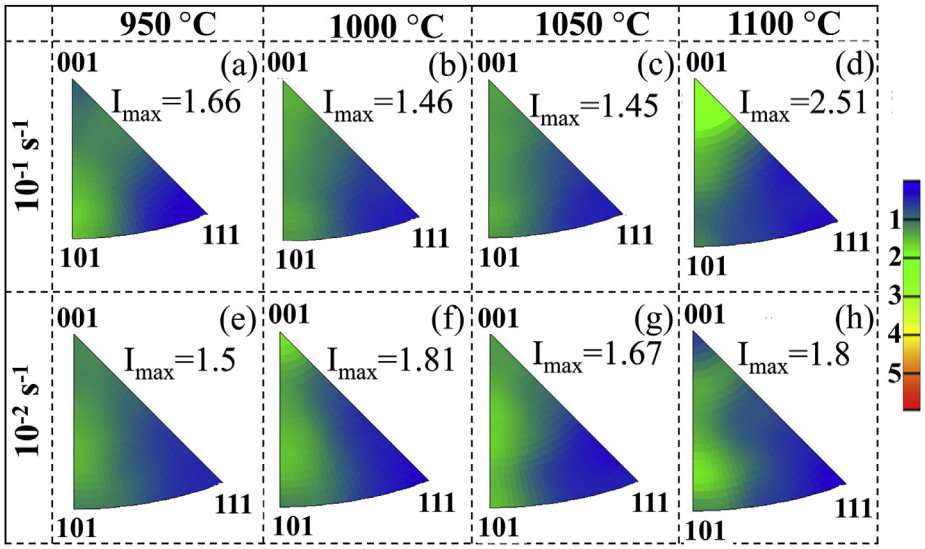

Fig. 16 – IPFs of recrystallized (DRX) grains obtained parallel to compression direction at different test conditions.

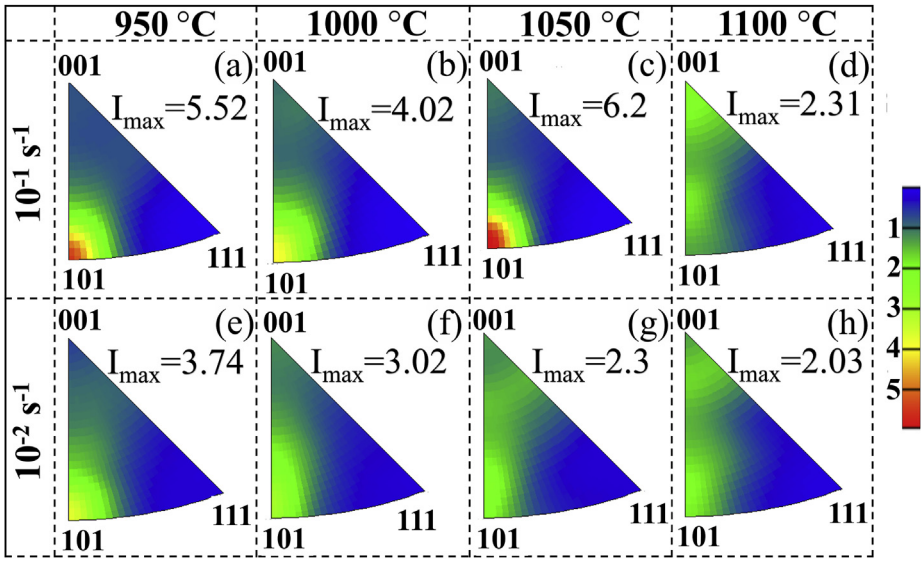

Fig. 17 – IPFs of un–recrystallized grains obtained parallel to compression direction at different test conditions.

dominance of the un–recrystallized grains fractions. The IPFs (Fig. 15) show the presence of <101> fiber texture due to a large fraction of un–recrystallized grains. However, at higher temperatures, a weak texture spreads towards <100> component. A similar behavior (with <100> and <111> components) of texture analysis is attributed to low SFE alloys, like CoCrFeMnNi HEA [14].

4. Conclusions

In this work the characteristics of DRX behavior in CoCrFeMnNi HEA has been investigated at strain rates 10^{-2} and 10^{-1} s^{-1} and in the temperature range of 950–1100 °C. The evolving microstructure and micro-texture have been analyzed in the light of deformation conditions. The conclusions from the present work were as follows:

1. As expected, the critical strain for the initiation of DRX process decreased with an increase in temperature at both the strains rates.
2. The values of k & n_c were estimated for the cantor alloy with the help of Avrami–type functions fitted to the experimental data at different deformation conditions in order to be able to predict the volume fraction of DRX (X_{DRX}) values.
3. The f_{DRX} values increased with the increase in deformation temperature at 10^{-1} s^{-1}, unlike in the case of hot deformation at $10^{-2}s^{-1}$, where the f_{DRX} value actually reduced with increase in temperature. This means that the DRX process was completed ($X_{DRX} = 1$) with the increase in temperature and a steady–state behavior was achieved at ~0.6, 0.5 and 0.45 strains for 1000, 1050 and 1100 °C temperatures respectively, deformed at 10^{-2} s^{-1}. Therefore, the evolved DRX grains experienced straining and dynamic equilibrium via dynamic restoration processes, which increased the average misorientation angle in course of steady–state flow.
4. The necklace structure along the grain boundaries shows the DDRX as a dominant DRX mechanism. The respective necklace structure comprises finely recrystallized grains in various stages of growth with substructure (LAGBs) and high local misorientation intensity.
5. Microtextural evolution quantified by IPFs revealed the evidence of the tendency towards <101> fiber compression texture formation and is observed to be most dominant among the un–recrystallized grains.

Data availability statement

Original data will be made available by the authors on request.

Declaration of Competing Interest

The authors declare that they have no known competing financial interests or personal relationships that could have appeared to influence the work reported in this paper.

Acknowledgement

Authors acknowledge TUNI Foundation as a part of Tampere university's graduate school and Encouragement grant from Finnish foundation of technology for financial support. In addition, this work made use of Tampere Microscopy Centre facilities at Tampere University. Authors sincere thank Juha Uusitalo and Jussi Paavola from University of Oulu for conducting Gleeble experiments and laboratory rolling.

REFERENCES

[1] Yeh J-W, Chen S-K, Lin S-J, Gan J-Y, Chin T-S, Shun T-T, et al. Nanostructured high-entropy alloys with multiple principal elements: novel alloy design concepts and outcomes. Adv Eng Mater 2004;6:299–303. https://doi.org/10.1002/adem.200300567.

[2] Murty BS, Yeh JW, Ranganathan S. High entropy alloys. Elsevier; 2014. https://doi.org/10.1016/B978-0-12-800251-3.00001-8.

[3] Miracle DB, Senkov ON. A critical review of high entropy alloys and related concepts. Acta Mater 2017;122:448–511. https://doi.org/10.1016/j.actamat.2016.08.081.

[4] George EP, Raabe D, Ritchie RO. High-entropy alloys. Nature Reviews Materials 2019;4. https://doi.org/10.1038/s41578-019-0121-4.

[5] Cantor B, Chang ITH, Knight P, Vincent AJB. Microstructural development in equiatomic multicomponent alloys. Mater Sci Eng, A 2004;375–377:213–8. https://doi.org/10.1016/j.msea.2003.10.257.

[6] Li Y, Li R, Peng Q. Enhanced surface bombardment resistance of the CoNiCrFeMn high entropy alloy under extreme irradiation flux. Nanotechnology 2020. https://doi.org/10.1088/1361-6528/ab473f.

[7] Patnamsetty M, Somani MC, Ghosh S, Ahmed S, Peura P. Processing map for controlling microstructure and unraveling various deformation mechanisms during hot working of CoCrFeMnNi high entropy alloy. Mater Sci Eng, A 2020;793:139840. https://doi.org/10.1016/j.msea.2020.139840.

[8] Humphreys FJ, Hatherly M. Chapter 13 - hot deformation and dynamic restoration. In: Humphreys FJ, hatherly MBT-R and RAP. Second E. Oxford: Elsevier; 2004. p. 415. https://doi.org/10.1016/B978-008044164-1/50017-7.

[9] Zaddach AJ, Scattergood RO, Koch CC. Tensile properties of low-stacking fault energy high-entropy alloys. Mater Sci Eng, A 2015;636:373–8. https://doi.org/10.1016/j.msea.2015.03.109.

[10] Huang S, Li W, Lu S, Tian F, Shen J, Holmström E, et al. Temperature dependent stacking fault energy of FeCrCoNiMn high entropy alloy. Scripta Mater 2015. https://doi.org/10.1016/j.scriptamat.2015.05.041.

[11] Haase C, Barrales-Mora LA. Influence of deformation and annealing twinning on the microstructure and texture evolution of face-centered cubic high-entropy alloys. Acta Mater 2018. https://doi.org/10.1016/j.actamat.2018.02.048.

[12] Skrotzki W, Pukenas A, Joni B, Odor E, Ungar T, Hohenwarter A, et al. Microstructure and texture evolution during severe plastic deformation of CrMnFeCoNi high-entropy alloy. IOP Conf Ser Mater Sci Eng 2017. https://doi.org/10.1088/1757-899X/194/1/012028.

[13] Laplanche G, Horst O, Otto F, Eggeler G, George EP. Microstructural evolution of a CoCrFeMnNi high-entropy alloy after swaging and annealing. J Alloys Compd 2015. https://doi.org/10.1016/j.jallcom.2015.05.129.

[14] Eleti RR, Bhattacharjee T, Zhao L, Bhattacharjee PP, Tsuji N. Hot deformation behavior of CoCrFeMnNi FCC high entropy alloy. Mater Chem Phys 2018;210:176–86. https://doi.org/10.1016/j.matchemphys.2017.06.062.

[15] Soares GC, Patnamsetty M, Peura P, Hokka M. Effects of adiabatic heating and strain rate on the dynamic response of a CoCrFeMnNi high-entropy alloy. J Dynamic Behavior Mater 2019;5:320–30. https://doi.org/10.1007/s40870-019-00215-w.

[16] Poliak EI, Jonas JJ. A one-parameter approach to determining the critical conditions for the initiation of dynamic recrystallization. Acta Mater 1996;44:127–36. https://doi.org/10.1016/1359-6454(95)00146-7.

[17] Chen B-R, Yeh A-C, Yeh J-W. Effect of one-step recrystallization on the grain boundary evolution of CoCrFeMnNi high entropy alloy and its subsystems. Sci Rep 2016;6:22306. https://doi.org/10.1038/srep22306.

[18] Masoumi M, Herculano LFG, Almeida AA, Béreš M, de Abreu HFG. Texture study across thickness of API X70 steel after hot deformation and different posttreatments. J Occup Med 2016;68:401–9. https://doi.org/10.1007/s11837-015-1712-1.

[19] Varela-Castro G, Cabrera J-M, Prado J-M. Critical strain for dynamic recrystallisation. The particular case of steels. Metals 2020;10:135. https://doi.org/10.3390/met10010135.

[20] Guo NN, Wang L, Luo LS, Li XZ, Chen RR, Su YQ, et al. Hot deformation characteristics and dynamic recrystallization of the MoNbHfZrTi refractory high-entropy alloy. Mater Sci Eng 2016;651:698–707. https://doi.org/10.1016/j.msea.2015.10.113.

[21] Ghosh S, Somani MC, Setman D, Mula S. Elucidation of deformation mechanisms and construction of processing maps for a Ti+Nb stabilized IF steel. Mater Sci Eng 2020. https://doi.org/10.1016/j.msea.2020.139648.

[22] zheng Quan G, Mao A, chang Luo G, ting Liang J, sen Wu D, Zhou J. Constitutive modeling for the dynamic recrystallization kinetics of as-extruded 3Cr20Ni10W2 heat-resistant alloy based on stress-strain data. Mater Des 2013;52:98–107. https://doi.org/10.1016/j.matdes.2013.05.030.

[23] Ghosh S, Somani MC, Setman D, Mula S. Hot deformation characteristic and strain dependent constitutive flow stress modelling of Ti + Nb stabilized interstitial free steel. Met Mater Int 2020. https://doi.org/10.1007/s12540-020-00827-1.

[24] Ryan ND, McQueen HJ. Dynamic softening mechanisms in 304 austenitic stainless steel. Canadian Metallurgical Quarterly 1990;29:147–62. https://doi.org/10.1179/cmq.1990.29.2.147.

[25] Jonas JJ, Quelennec X, Jiang L, Martin É. The Avrami kinetics of dynamic recrystallization. Acta Mater 2009;57:2748–56. https://doi.org/10.1016/j.actamat.2009.02.033.

[26] Mandal S, Jayalakshmi M, Bhaduri AK, Subramanya Sarma V. Effect of strain rate on the dynamic recrystallization behavior in a nitrogen-enhanced 316L(N). Metall Mater Trans: Physical Metallurgy and Materials Science 2014. https://doi.org/10.1007/s11661-014-2480-1.

[27] Humphreys FJ, Hatherly M. In: Humphreys FJ, Hatherly MBT-R, editors. Chapter 14 - continuous recrystallization during and after large strain deformation. Oxford: Elsevier; 2004. p. 451–67. https://doi.org/10.1016/B978-008044164-1/50018-9.

[28] Ravichandran N, Prasad YVRK. Dynamic recrystallization during hot deformation of aluminum: a study using processing maps. Metallurgical Transactions A 1991;22:2339–48. https://doi.org/10.1007/BF02665000.

[29] Kumar SSS, Raghu T, Bhattacharjee PP, Appa Rao G, Borah U. Evolution of microstructure and microtexture during hot deformation in an advanced P/M nickel base superalloy. Mater Char 2018;146:217–36. https://doi.org/10.1016/j.matchar.2018.10.008.

[30] Huang K, Logé RE. A review of dynamic recrystallization phenomena in metallic materials. Mater Des 2016. https://doi.org/10.1016/j.matdes.2016.09.012.

[31] Patnamsetty M, Saastamoinen A, Somani MC, Peura P. Constitutive modelling of hot deformation behaviour of a CoCrFeMnNi high-entropy alloy. Sci Technol Adv Mater 2020;21:43–55. https://doi.org/10.1080/14686996.2020.1714476.

[32] Kodzhaspirov GE, Terentyev MI. Modeling the dynamically recrystallized grain size evolution of a superalloy. Mater Phys Mech 2012;13:84.

[33] Wu H, Liu M, Wang Y, Huang Z, Tan G, Yang L. Experimental study and numerical simulation of dynamic recrystallization for a FGH96 superalloy during isothermal compression. J Mater Research Technol 2020;9:5090–104. https://doi.org/10.1016/j.jmrt.2020.03.026.

[34] Du S, Chen S, Song J, Li Y. Hot deformation behavior and dynamic recrystallization of medium carbon LZ50 steel. Metall Mater Trans 2017;48:1310–20. https://doi.org/10.1007/s11661-016-3938-0.
[35] Liu YG, Li MQ, Luo J. The modelling of dynamic recrystallization in the isothermal compression of 300M steel. Mater Sci Eng 2013. https://doi.org/10.1016/j.msea.2013.03.011.
[36] Dehghan-Manshadi A, Barnett MR, Hodgson PD. Hot deformation and recrystallization of austenitic stainless steel: Part I. Dynamic recrystallization. Metall Mater Trans 2008;39:1359–70. https://doi.org/10.1007/s11661-008-9512-7.
[37] Chen L, Sun W, Lin J, Zhao G, Wang G. Modelling of constitutive relationship, dynamic recrystallization and grain size of 40Cr steel during hot deformation process. Results in Physics 2019;12:784–92. https://doi.org/10.1016/j.rinp.2018.12.046.
[38] Tóth LS, Estrin Y, Lapovok R, Gu C. A model of grain fragmentation based on lattice curvature. Acta Mater 2010. https://doi.org/10.1016/j.actamat.2009.11.020.